

Quantum-inspired Chemical Rule for Discovering Topological Materials

Xinyu Xu,¹ Rajibul Islam,² Ghulam Hussain,³ Yangming Huang,⁴ Xiaoguang Li,³ Pavlo O. Dral,⁴ Arif Ullah,^{1, a)} and Ming Yang^{1, b)}

¹⁾ School of Physics, Anhui University, Hefei 230601, China

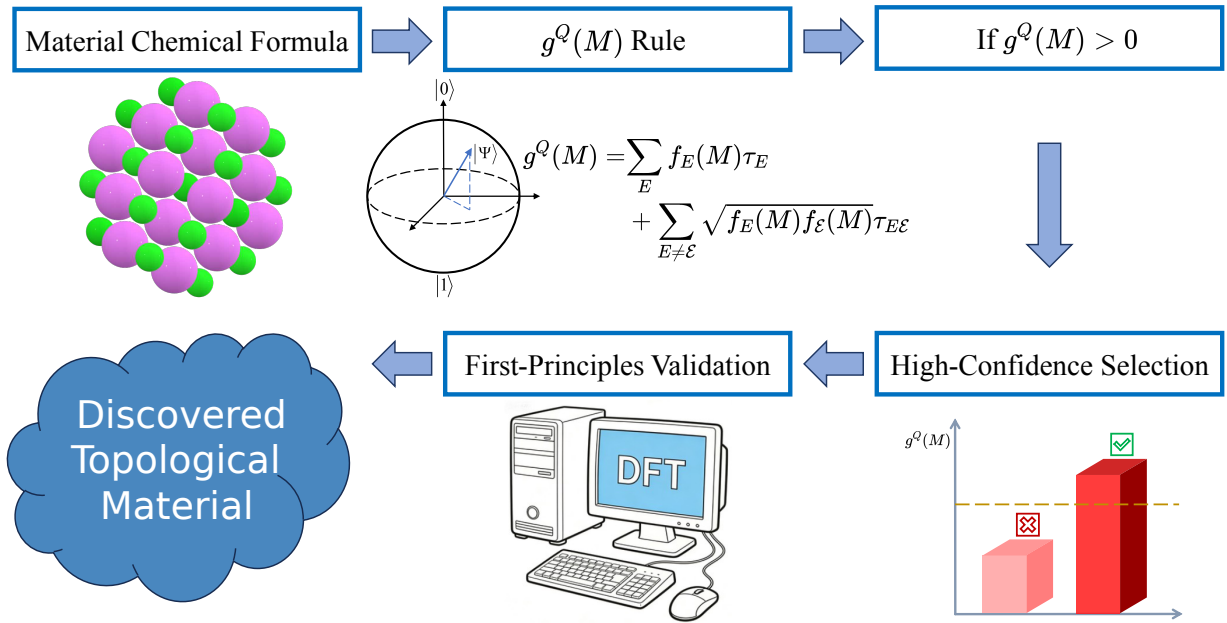
²⁾ Department of Physics, University of Alabama at Birmingham, Birmingham 35294, AL, USA

³⁾ Institute for Advanced Study, Shenzhen University, Shenzhen 518060, China

⁴⁾ State Key Laboratory of Physical Chemistry of Solid Surfaces, College of Chemistry and Chemical Engineering, Fujian Provincial Key Laboratory of Theoretical and Computational Chemistry, and Innovation Laboratory for Sciences and Technologies of Energy Materials of Fujian Province (IKKEM), Xiamen University, Xiamen, 361005, Fujian, China

(Dated: 16 December 2025)

Topological materials exhibit unique electronic structures that underpin both fundamental quantum phenomena and next-generation technologies, yet their discovery remains constrained by the high computational cost of first-principles calculations and the slow, resource-intensive nature of experimental synthesis. Recent machine-learning approaches, such as the heuristic topogivity rule, offer data-driven alternatives by quantifying each element's intrinsic tendency toward topological behavior. Here, we develop a quantum–classical hybrid artificial neural network (QANN) that extends this rule into a quantum-inspired formulation. Within this framework, the QANN maps compositional descriptors to quantum probability amplitudes, naturally introducing pairwise inter-element correlations inaccessible to classical heuristics. The physical validity of these correlations is substantiated by constructing an equivalent complex-valued neural network (CVNN), confirming both the consistency and interpretability of the formulation. Retaining the simplicity of chemical reasoning while embedding quantum-native features, our quantum-inspired rule enables efficient and generalizable topological classification. High-throughput screening combined with first-principles (DFT) validation reveals five previously unreported topological compounds, demonstrating the enhanced predictive power and physical insight afforded by quantum-inspired heuristics.



Topological materials are a vast category of quantum matter where the electronic wave functions possess non-trivial topological structures defined by quantized

invariants.^{1–5} This family includes topological insulators (TIs), which feature an insulating interior but symmetry-protected metallic surface states,^{6–13} and topological semimetals (TSMs), which host distinctive Weyl or Dirac nodes characterized by Berry-curvature textures.^{14–18} The robust boundary modes in these materials lead to hallmark quantum responses—such as the quantum spin Hall effect¹⁹ and anomalous transport²⁰—that are highly

^{a)} Electronic mail: arif@ahu.edu.cn

^{b)} Electronic mail: mingyang@ahu.edu.cn

promising for next-generation nanoscale quantum and spintronic technologies. To fully exploit the potential of these functional quantum materials, the primary obstacle is the development of efficient and universal criteria for reliably identifying whether a given compound has a topologically non-trivial electronic structure.

Traditional discovery paradigms rely on the synergy between first-principles electronic structure calculations and topological band theory, where topological invariants are directly computed from Bloch wave functions.^{21,22} Over the past decade, this foundation has been systematized through the development of topological quantum chemistry (TQC)²³ and symmetry indicator (SI) approaches.^{24–28} These frameworks link symmetry eigenvalues at high-symmetry points to the global topology of electronic bands, thereby enabling large-scale, high-throughput screening of candidate topological materials.^{29–31} Their success has established symmetry-based methods as indispensable tools in modern topological materials discovery.

However, symmetry-based diagnostics are inherently incomplete. They are limited to crystalline systems where symmetry representations are well defined and cannot universally capture topological phases arising from accidental band inversions, low-symmetry distortions, or strong spin-orbit interactions beyond perturbative regimes. A paradigmatic example is the Weyl semimetal TaAs,^{15,16} whose topological character cannot be inferred from symmetry indicators alone but requires explicit computation of Berry curvature and Chern numbers from wave functions.³² Similar challenges arise for Chern insulators lacking point-group symmetry and time-reversal-invariant Z_2 topological insulators, where direct evaluation of topological invariants remains indispensable. These limitations underscore a fundamental bottleneck: the absence of a unified and generalizable framework capable of identifying topological character across materials of arbitrary symmetry, chemical complexity, and correlation strength.

In the past decade, the rapid advancement of machine learning (ML) has introduced a powerful new paradigm for materials discovery, including the prediction of topological phases^{33–41} and topological invariants directly from electronic or structural descriptors.^{42–44} Within this growing body of work, Ma et al.³⁸ proposed a particularly elegant approach that parallels the heuristic reasoning of chemistry: a data-driven chemical rule for diagnosing electronic topology that operates independently of crystalline symmetry. Instead of relying on opaque “black-box” models, their method introduces a machine-learned elemental descriptor—termed topogivity—which quantifies each element’s intrinsic tendency to participate in topological phases. The topological nature of a compound can then be inferred from the sign of the composition-weighted average of its constituent elements’ topogivities, providing a simple yet remarkably effective heuristic that bridges atomic chemistry and topological quantum physics.

In recent years, quantum computers have emerged as a promising platform for simulating and understanding complex quantum systems that are intractable on classical hardware.^{45,46} Their inherent ability to represent and manipulate quantum states directly offers a natural framework for modeling materials whose essential physics is quantum mechanical in nature—particularly those involving strong correlations and topological phases. Parallel to the rise of quantum hardware, the field of quantum machine learning (QML) has developed rapidly, integrating concepts from both quantum computation and classical data-driven learning.⁴⁷ QML models, operating in high-dimensional Hilbert spaces, can in principle capture entanglement and coherence effects beyond the reach of classical neural networks,^{48,49} thus providing a fundamentally quantum approach to pattern recognition and materials prediction. Motivated by these advances, we aim to extend topogivity-based heuristic rule for topological materials discovery into the quantum domain, developing hybrid frameworks that exploit both chemical intuition and quantum-native representations.

In this work, we introduce a quantum-inspired chemical rule, $g^Q(M)$, derived from a quantum-classical hybrid artificial neural network (QANN) (Fig. 1c) designed to incorporate quantum advantages into the identification of topological materials. Unlike the classical heuristic of Ma et al.,³⁸ which assigns an independent scalar propensity to each element, $g^Q(M)$ embeds pairwise correlation terms that encode inter-element quantum interactions absent in conventional models. The structure of these correlations is further validated using an equivalent complex-valued neural network (CVNN), which independently reproduces the same analytical form and reinforces the interpretability of the rule.

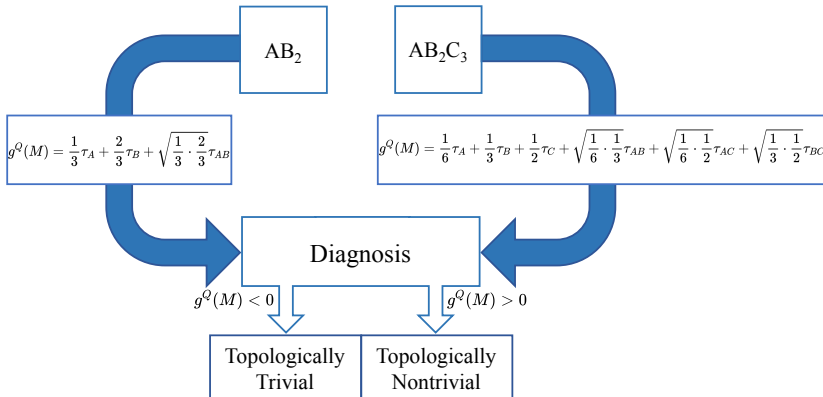
For practical screening, a material is classified as topological when $g^Q(M) > 0$ and trivial when $g^Q(M) < 0$ (Fig. 1a). Applying this rule in a high-throughput workflow, we screened a large materials database and performed first-principles (DFT) verification of representative predictions (Fig. 1b). Importantly, this quantum-inspired approach identifies five previously unreported topological materials overlooked by the classical counterpart, demonstrating its enhanced discovery capability and value for accelerating materials design.

We begin by introducing the central outcome of this study—the quantum-inspired chemical rule $g^Q(M)$, expressed as:

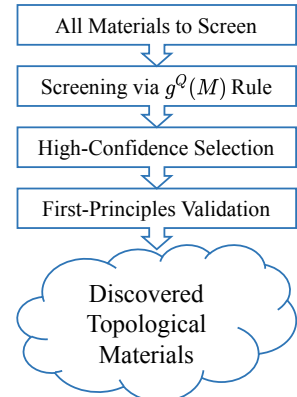
$$\begin{aligned} g^Q(M) &= \sum_E f_E(M)\tau_E + \sum_{E \neq \mathcal{E}} \sqrt{f_E(M)f_{\mathcal{E}}(M)}\tau_{E\mathcal{E}} \\ &= g(M) + \sum_{E \neq \mathcal{E}} \sqrt{f_E(M)f_{\mathcal{E}}(M)}\tau_{E\mathcal{E}}, \end{aligned} \quad (1)$$

where the sum runs over all elements appearing in the chemical formula of material M , and $f_E(M)$ denotes the fractional abundance of element E . The parameters τ_E represent element-specific contributions (the topogivity

(a) Quantum-Inspired Chemical Rule



(b) High-Throughput Discovery



(c) Workflow of the QANN Model

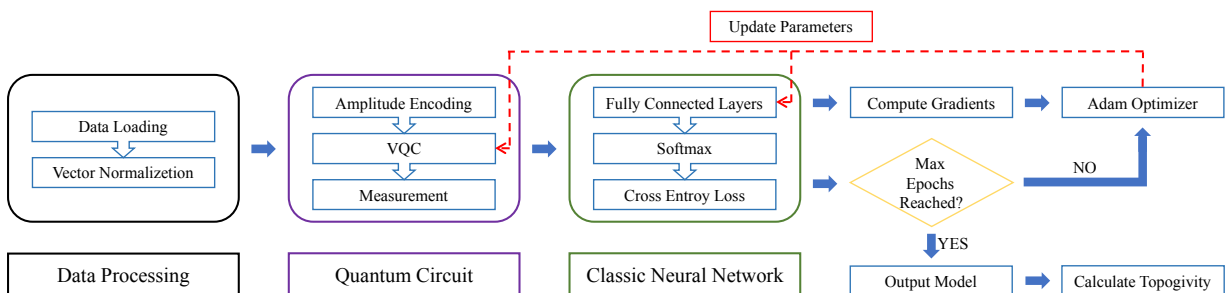


FIG. 1: QANN-based diagnosis and discovery of topological materials. **(a)** Schematic illustration of the quantum-inspired heuristic rule $g^Q(M)$ for topological diagnosis. For a given compound (e.g., AB_2 or AB_2C_3), the diagnostic value is obtained in two steps: first, by computing the weighted average of the constituent elements' topogivities (τ_A, τ_B, τ_C) according to their stoichiometric ratios; and second, by evaluating the weighted average of pairwise quantum topogivities ($\tau_{AB}, \tau_{AC}, \tau_{BC}$) between distinct elements, with weights given by the product of their relative abundances. The overall diagnostic value—sum of the two contributions—encodes both the topological classification (sign) and the confidence level (magnitude). **(b)** High-throughput discovery workflow using quantum-inspired chemical rule. Chemical formulae are first used for topological property prediction, followed by screening of high-confidence candidates. The shortlisted materials are then validated via DFT calculations, leading to the identification of previously unreported topological materials. **(c)** The general workflow of our QANN model, which integrates data preprocessing, a quantum circuit, and a classical neural network. Further details are given in Section S1 of the Supporting Information (SI).

of E), while $\tau_{E\mathcal{E}}$ capture pairwise interactions between distinct elements E and \mathcal{E} . For example, in a ternary compound $A_xB_yC_z$, the elemental fractions are $f_A(M) = \frac{x}{x+y+z}$, $f_B(M) = \frac{y}{x+y+z}$, and $f_C(M) = \frac{z}{x+y+z}$. In this case, the rule depends on both the individual topogivities τ_A , τ_B , and τ_C , as well as the interaction parameters τ_{AB} , τ_{AC} , and τ_{BC} , as illustrated in Fig. 1. The full derivation of $g^Q(M)$ rule is provided in Section S1 of the Supporting Information (SI), and its complex-valued-network counterpart in Section S2.

In Eq.(1), the first term recovers the purely classical rule proposed by Ma et al.³⁸, while the second term represents the additional contribution originating from the quantum part of our QANN model. The classification decision is determined by the sign of $g^Q(M)$. If $g^Q(M)$

is positive, the material is classified as topologically non-trivial. If $g^Q(M)$ is negative, it is classified as topologically trivial. A larger absolute value of $g^Q(M)$ generally indicates a higher confidence level in the classification judgment.

We adopt a supervised learning approach to derive chemically inspired rules for diagnosing topological materials. Our training dataset is taken from Ma et al.³⁸, which itself was curated from a subset of the database compiled by Tang et al.²⁹.

The dataset contains 9,026 materials, of which 51% are labeled as topologically trivial and 49% as non-trivial (combining topological insulators and topological semimetals into a single category), spanning a total of 54 distinct elements. As shown in Fig. 3(a), the materials are distributed across compounds containing one

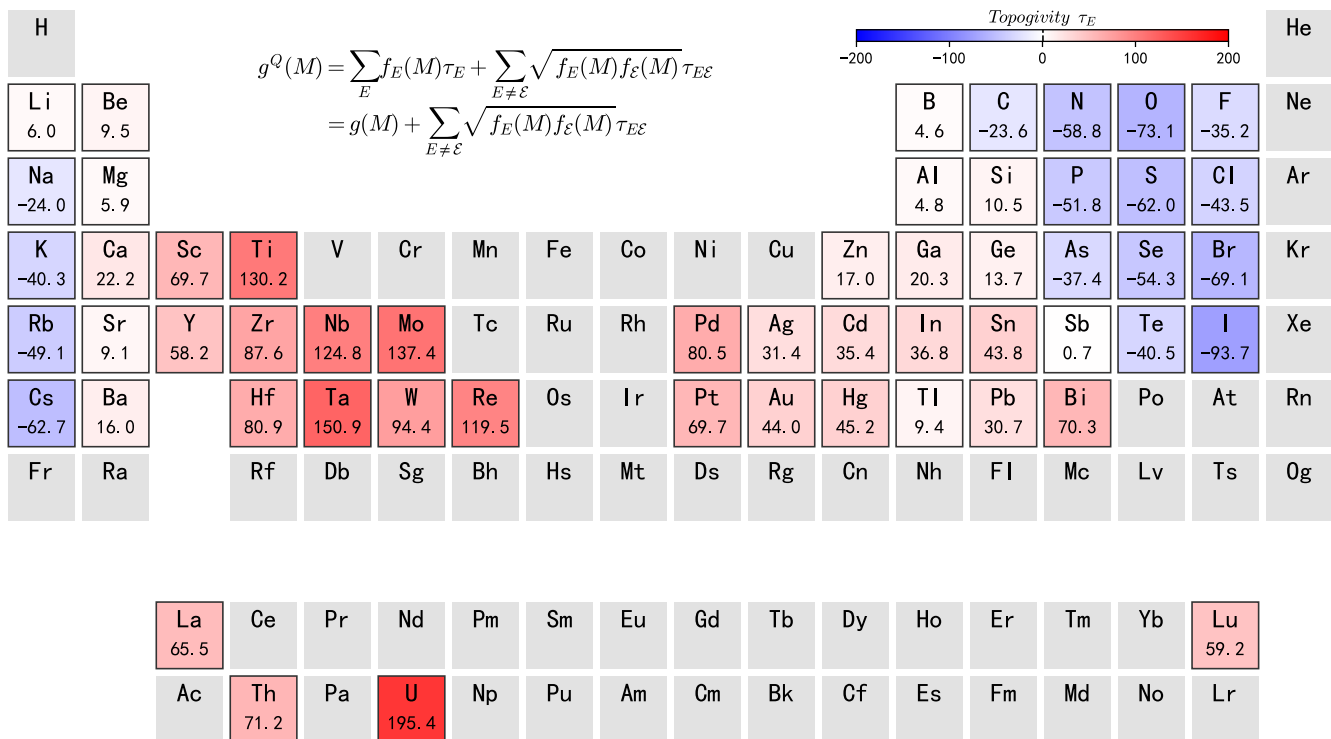


FIG. 2: Periodic table of topogivities. Color-coding and numerical values represent QANN topogivities τ_E . Gray elements indicate those not present in the dataset. The complete model contains 1,485 topogivity values (54 elemental topogivities shown here plus 1,431 cross-correlation terms not included in the periodic table representation).

to six elements, with counts of 213, 3,317, 4,483, 944, 67, and 2, respectively; the corresponding percentages of topological materials in each group are 76.5%, 69.1%, 40.6%, 14.7%, 13.4%, and 0.0%. As noted in Ref. 38, the dataset is inherently noisy because symmetry-based high-throughput methods cannot capture all topological states, meaning some topological materials may be mislabeled as trivial. In addition, we consider a discovery set of 1,433 materials, also from Ma et al., whose topological character cannot be determined by symmetry indicators. Our approach applies the $g^Q(M)$ chemical rule to this discovery set, followed by DFT validation of materials whose predictions differ from Ref. 38, enabling an assessment of the rule’s predictive performance.

Each dataset entry includes a material’s chemical formula, space group (SG), and topological label, with non-trivial materials labeled 1 and trivial ones labeled 0. Since our chemical rule is symmetry-agnostic, only chemical formulas and labels are used for training. Labels are converted into one-hot vectors—[0,1] for nontrivial and [1,0] for trivial—to facilitate model learning.

To evaluate the predictive capability of our quantum-inspired chemical rule, we apply Eq. (1) to classify materials in terms of their topological or trivial character.

Prior to screening the 1,433-material discovery set, we assess performance on the full labeled dataset of 9,026 materials. From this dataset, 8,000 materials are used for training, while the remaining 1,026 compounds serve as an independent hold-out test set.

We train our model using 10-fold cross-validation on the 8,000-material training subset. Each fold produces a full set of learned topogivities and pairwise correlation parameters; these ten parameter sets are subsequently normalized and averaged to obtain the final chemical rule used throughout this work (see Section S3 of the SI for details).

Figure 2 displays the periodic-table distribution of the learned topogivities. The trends are chemically intuitive: elements with strong spin-orbit coupling—such as Ta, Nb, and Mo—exhibit strongly positive topogivities, consistent with their known tendency to support topological electronic phases. Conversely, light elements (Li, Be, B) contribute only weakly, while nonmetals and halogens show pronounced negative values, reflecting their frequent association with electronically trivial systems.

Figure 3(b) summarizes the model’s performance across cross-validation and on the final independent test set. The averaged metrics demonstrate consistently

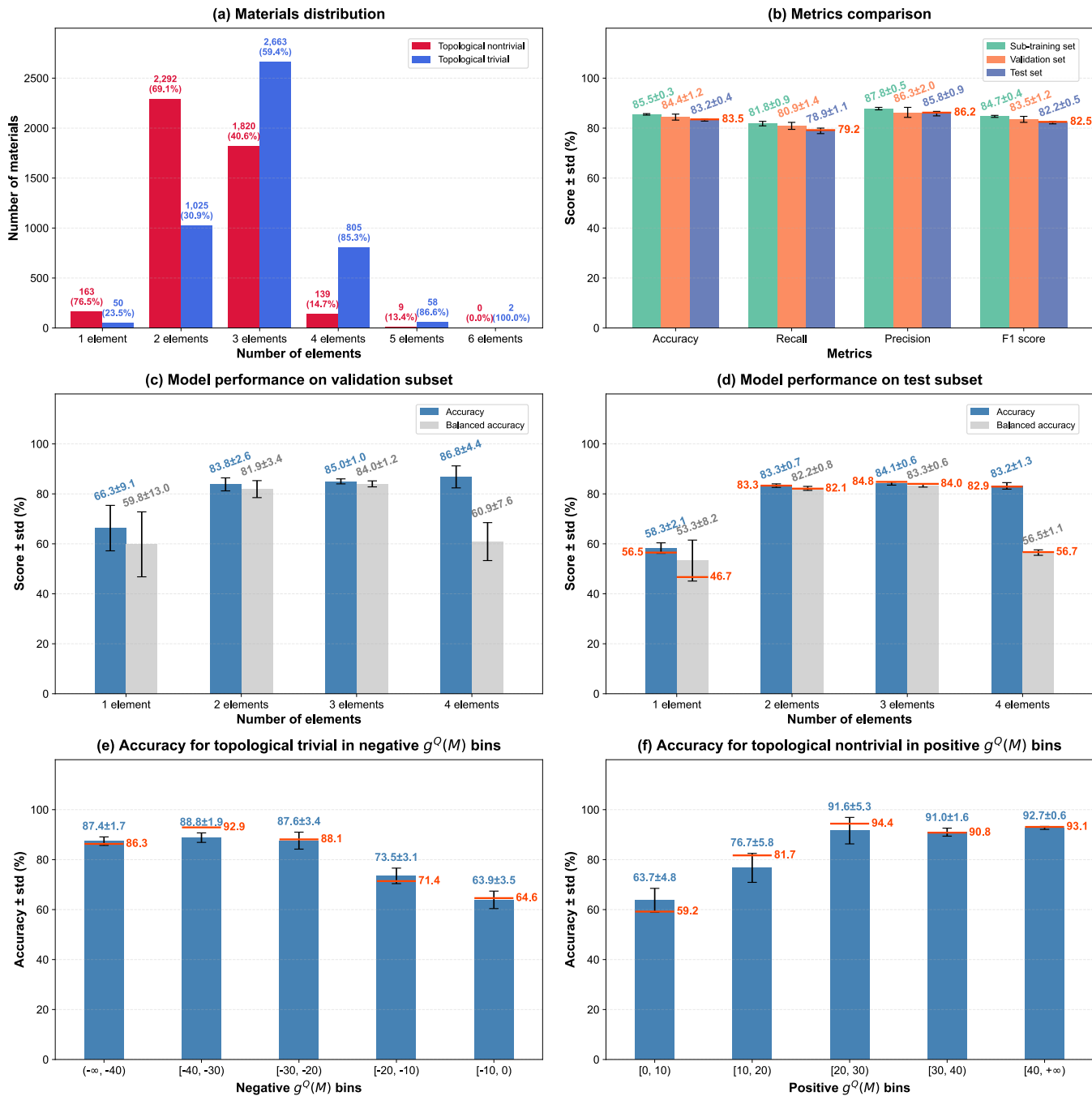


FIG. 3: Model performance and dataset analysis. (a) Distribution of labeled materials grouped by elemental complexity (binary, ternary, quaternary, etc.). (b) Summary of model performance in 10-fold cross-validation and on the final held-out test set (reported as mean \pm standard deviation (std) across folds). (c) Cross-validation accuracy and balanced accuracy, averaged over 10 folds, resolved by material complexity (element count). (d) Generalization performance on the independent test set: accuracy and balanced accuracy as functions of material elemental count. (e) Test-set accuracy for topologically trivial compounds within negative $g^Q(M)$ bins. (f) Test-set accuracy for topologically nontrivial compounds within positive $g^Q(M)$ bins. In panels (b) and (d)–(f), the red line shows the score obtained on the final test set using the aggregated parameter values employed to compute $g^Q(M)$.

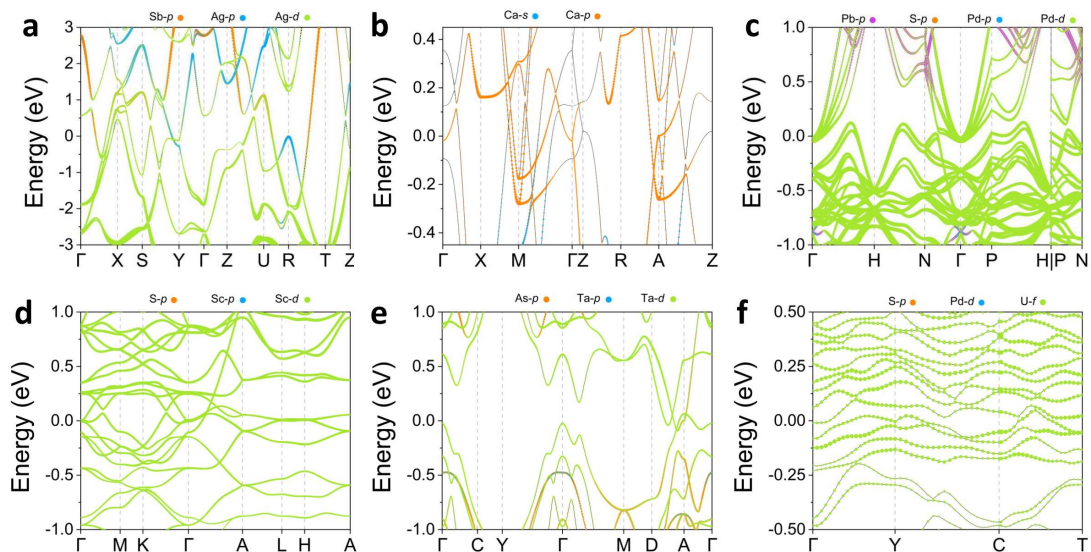


FIG. 4: Orbital projected electronic band structures of representative compounds illustrating diverse topological behaviors for (a) Ag_3Sb , (b) Ca , (c) $\text{Pd}_3(\text{PbS})_2$, (d) P_3Sc_7 , (e) As_2Ta , and (f) PdS_4U_2 .

strong predictive capacity across folds. On the final 1,026-material test set, the learned chemical rule achieves 83.5% accuracy, 79.2% recall, 86.2% precision, and an F1 score of 82.5%, indicating reliable generalization to unseen materials.

We further analyze accuracy and balanced accuracy as functions of compositional complexity (Fig. 3(c)–(d)). Because five- and six-element materials are extremely rare in the labeled dataset, we restrict our analysis to compounds with one to four distinct elements to ensure that each validation fold contains both trivial and topological samples. The model performs most robustly for binary and ternary materials, which constitute the majority of the dataset. For one-element and four-element compounds, the accuracy remains relatively high; however, the balanced accuracy drops significantly for four-element systems. This discrepancy arises from the strong label imbalance evident in Fig. 3(a), where the fraction of topological materials decreases markedly as the number of constituent elements increases. As a consequence, accuracy alone becomes misleading, reinforcing the necessity of reporting balanced accuracy in this setting. On the independent test set (Fig. 3(d)), the learned rule achieves 83.3% accuracy for binary materials and 84.8% for ternary materials.

Finally, Fig. 3(e)–(f) provides an uncertainty-resolved analysis based on the magnitude of $g^Q(M)$. The model exhibits high accuracy and minimal standard deviation for $|g^Q(M)| > 20$, where classifications are consistently reliable. In the intermediate region $-20 < g^Q(M) < 20$, the accuracy decreases and the standard deviation increases, reflecting intrinsically higher classification uncertainty near the decision boundary. This behavior supports the use of $|g^Q(M)| > 20$ as a practical high-confidence threshold for screening applications. Ad-

ditional confidence-score analysis from the topological-phase perspective is provided in Section S4 of the SI, further clarifying the reliability regions of the $g^Q(M)$ rule.

For the high-throughput screening stage, we applied our quantum-inspired diagnostic function, $g^Q(M)$, to all 1,433 materials in the discovery space. Each material’s topological character was first assessed based on its $g^Q(M)$ value. Based on the diagnostic results, among the 142 materials initially identified as topological (i.e., $g^Q(M) > 0$), we screened 79 materials that satisfied the high-confidence topologically nontrivial classification criterion (i.e., $g^Q(M) \geq 20$).

Following the screening strategy adopted in Ref. 38, we excluded seven compounds from the candidate list, resulting in a refined set of 72 high-priority materials for subsequent first-principles validation.

Of these, 66 materials had already been examined in Ref. 38, where 56 were confirmed to be topological. We therefore concentrated our computational efforts on the six previously unvalidated candidates: Ca (SG 92), As_2Ta (SG 12), Ag_3Sb (SG 25), P_3Sc_7 (SG 186), $\text{Pd}_3(\text{PbS})_2$ (SG 199), and PdS_4U_2 (SG 43). For these compounds, DFT calculations were performed using the VASP package.^{50,51} Core and valence electrons were treated using the projector-augmented wave (PAW) method with a plane-wave cutoff energy of 600 eV.⁵² Structural relaxations were conducted until forces were below 0.001 eV/Å and total-energy changes were less than 10^{-8} eV. A k -mesh commensurate with each lattice was used, and all electronic structure calculations included SOC.

As shown in Fig. 4, our calculations verified that five of these six compounds exhibit topological semimetal characteristics (Fig. 4(a)–(e)), with PdS_4U_2 identified as a topologically trivial metal ((Fig. 4(f)). Altogether,

our quantum-inspired diagnostic framework successfully identified 61 topological materials: the 56 previously validated in Ref. 38 and five newly discovered through our approach. Furthermore, our method reduces the number of false positives by two relative to the screening workflow of Ref. 38, achieving an overall prediction accuracy of 84.7%.

In conclusion, we have introduced a quantum-inspired chemical rule derived from a quantum-classical hybrid network that generalizes the classical ML-based element-specific topogivity concept into the quantum domain. By incorporating pairwise, quantum-motivated correlation terms between elements, the framework requires only the chemical composition of a material yet enables high-throughput, coarse-grained, and remarkably accurate diagnosis of topological character. This rule provides an efficient front-end filter for large-scale materials screening, identifying promising candidates for first-principles calculations and experimentally demanding validation. In doing so, it reduces computational cost, accelerates materials discovery, and offers an accessible diagnostic tool for researchers without extensive prior expertise in topological materials. Importantly, the approach remains applicable even to compounds that cannot be diagnosed using symmetry-indicator methods.

The proposed rule serves as a natural, quantum-mechanically informed extension of the original topogivity framework. By moving beyond single-element scores to explicitly capturing inter-element interactions, it shifts the perspective from describing which elements constitute a material to inferring how these elements may interact to give rise to topological behavior. This enhancement brings the model closer to the underlying physico-chemical mechanisms responsible for topological phases.

Future efforts may extend this framework by integrating additional descriptors—such as space group, total and valence electron counts, or chemical family information (e.g., alkali metals, halogens)—to further improve classification accuracy. Moreover, applying the quantum-inspired rule to larger and more diverse materials databases will not only expand its discovery potential but also deepen our understanding of elemental contributions and quantum-originated cross-correlation patterns in topological materials.

I. SUPPORTING INFORMATION

Derivation of quantum-inspired chemical rules based on the QANN model, validation with CVNN, detailed training specifications, and confidence analysis of the $g^Q(M)$ score.

II. ACKNOWLEDGMENTS

A.U. acknowledges funding from the National Natural Science Foundation of China (No. W2433037) and

the Natural Science Foundation of Anhui Province (No. 2408085QA002).

REFERENCES

- ¹F. D. M. Haldane, *Phys. Rev. Lett.* **61**, 2015 (1988).
- ²C. L. Kane and E. J. Mele, *Phys. Rev. Lett.* **95**, 146802 (2005).
- ³M. Z. Hasan and C. L. Kane, *Rev. Mod. Phys.* **82**, 3045 (2010).
- ⁴X.-L. Qi and S.-C. Zhang, *Rev. Mod. Phys.* **83**, 1057 (2011).
- ⁵N. P. Armitage, E. J. Mele, and A. Vishwanath, *Rev. Mod. Phys.* **90**, 015001 (2018).
- ⁶C. L. Kane and E. J. Mele, *Phys. Rev. Lett.* **95**, 226801 (2005).
- ⁷B. A. Bernevig, T. L. Hughes, and S.-C. Zhang, *Science* **314**, 1757 (2006).
- ⁸M. König, S. Wiedmann, C. Brune, A. Roth, H. Buhmann, L. W. Molenkamp, X.-L. Qi, and S.-C. Zhang, *Science* **318**, 766 (2007).
- ⁹L. Fu, C. L. Kane, and E. J. Mele, *Phys. Rev. Lett.* **98**, 106803 (2007).
- ¹⁰D. Hsieh, D. Qian, L. Wray, Y. Xia, Y. S. Hor, R. J. Cava, and M. Z. Hasan, *Nature* **452**, 970 (2008).
- ¹¹L. Fu, *Phys. Rev. Lett.* **106**, 106802 (2011).
- ¹²T. H. Hsieh, H. Lin, J. Liu, W. Duan, A. Bansil, and L. Fu, *Nat. Commun.* **3**, 982 (2012).
- ¹³W. A. Benalcazar, B. A. Bernevig, and T. L. Hughes, *Science* **357**, 61 (2017).
- ¹⁴Z. K. Liu, B. Zhou, Y. Zhang, Z. J. Wang, H. M. Weng, D. Prabhakaran, S.-K. Mo, Z. X. Shen, Z. Fang, X. Dai, *et al.*, *Science* **343**, 864 (2014).
- ¹⁵S.-Y. Xu, I. Belopolski, N. Alidoust, M. Neupane, G. Bian, C. Zhang, R. Sankar, G. Chang, Z. Yuan, C.-C. Lee, *et al.*, *Science* **349**, 613 (2015).
- ¹⁶B. Q. Lv, H. M. Weng, B. B. Fu, X. P. Wang, H. Miao, J. Ma, P. Richard, X. C. Huang, L. X. Zhao, G. F. Chen, *et al.*, *Phys. Rev. X* **5**, 031013 (2015).
- ¹⁷A. A. Burkov, M. D. Hook, and L. Balents, *Phys. Rev. B* **84**, 235126 (2011).
- ¹⁸B. Bradlyn, J. Cano, Z. Wang, M. G. Vergniory, C. Felser, R. J. Cava, and B. A. Bernevig, *Science* **353**, aaf5037 (2016).
- ¹⁹C. L. Kane and E. J. Mele, *Phys. Rev. Lett.* **95**, 226801 (2005).
- ²⁰X.-L. Qi and S.-C. Zhang, *Rev. Mod. Phys.* **83**, 1057 (2011).
- ²¹J. Xiao and B. Yan, *Nat. Rev. Phys.* **3**, 283 (2021).
- ²²A. Bansil, H. Lin, and T. Das, *Rev. Mod. Phys.* **88**, 021004 (2016).
- ²³B. Bradlyn, L. Elcoro, J. Cano, M. G. Vergniory, Z. Wang, C. Felser, M. I. Aroyo, and B. A. Bernevig, *Nature* **547**, 298 (2017).
- ²⁴R.-J. Slager, A. Mesaros, V. Juričić, and J. Zaanen, *Nature Physics* **9**, 98 (2013).
- ²⁵H. C. Po, A. Vishwanath, and H. Watanabe, *Nat. Commun.* **8**, 50 (2017).
- ²⁶L. Fu and C. L. Kane, *Phys. Rev. B* **76**, 045302 (2007).
- ²⁷J. Kruthoff, J. de Boer, J. van Wezel, C. L. Kane, and R.-J. Slager, *Phys. Rev. X* **7**, 041069 (2017).
- ²⁸Z. Song, T. Zhang, Z. Fang, and C. Fang, *Nat. Commun.* **9**, 3530 (2018).
- ²⁹F. Tang, H. C. Po, A. Vishwanath, and X. Wan, *Nature* **566**, 486 (2019).
- ³⁰T. Zhang, Y. Jiang, Z. Song, H. Huang, Y. He, Z. Fang, H. Weng, and C. Fang, *Nature* **566**, 475 (2019).
- ³¹M. G. Vergniory, L. Elcoro, C. Felser, N. Regnault, B. A. Bernevig, and Z. Wang, *Nature* **566**, 480 (2019).
- ³²H. Weng, C. Fang, Z. Fang, B. A. Bernevig, and X. Dai, *Phys. Rev. X* **5**, 011029 (2015).
- ³³N. Claussen, B. A. Bernevig, and N. Regnault, *Phys. Rev. B* **101**, 245117 (2020).

- ³⁴G.-H. Cao, R.-H. Ouyang, L. M. Ghiringhelli, M. Scheffler, H.-J. Liu, C. Carbogno, and Z.-Y. Zhang, *Phys. Rev. Mater.* **4**, 034204 (2020).
- ³⁵H. Liu, S. Meng, and F. Liu, *Phys. Rev. Mater.* **5**, 084203 (2021).
- ³⁶G. R. Schleder, B. Focassio, and A. Fazzio, *Appl. Phys. Rev.* **8**, 031413 (2021).
- ³⁷N. Andrejevic, J. Andrejevic, B. A. Bernevig, N. Regnault, F. Han, G. Fabbris, T. Nguyen, N. C. Drucker, C. H. Rycroft, and M. Li, *Adv. Mater.* **34**, 2204113 (2022).
- ³⁸A. Ma, Y. Zhang, T. Christensen, H. C. Po, L. Jing, L. Fu, and M. Soljačić, *Nano Lett.* **23**, 772 (2023).
- ³⁹H.-S. Xu, Y.-D. Jiang, H. Wang, and J. Wang, *Phys. Rev. B* **109**, 115416 (2024).
- ⁴⁰X. Haosheng, Q. Dongheng, and W. Jing, *Chin. Phys. Lett.* **42**, 070706 (2025).
- ⁴¹A. Ullah, R. Islam, G. Hussain, Z. Muhammad, X. Li, and M. Yang, arXiv <https://doi.org/10.48550/arXiv.2511.04068> (2025), arXiv:2511.04068.
- ⁴²Y. Zhang and E.-A. Kim, *Phys. Rev. Lett.* **118**, 216401 (2017).
- ⁴³P.-F. Zhang, H. Shen, and H. Zhai, *Phys. Rev. Lett.* **120**, 066401 (2018).
- ⁴⁴M. S. Scheurer and R.-J. Slager, *Phys. Rev. Lett.* **124**, 226401 (2020).
- ⁴⁵R. P. Feynman, *Int. J. Theor. Phys.* **21**, 467 (1982).
- ⁴⁶I. M. Georgescu, S. Ashhab, and F. Nori, *Rev. Mod. Phys.* **86**, 153 (2014).
- ⁴⁷J. Biamonte, P. Wittek, N. Pancotti, P. Rebentrost, N. Wiebe, and S. Lloyd, *Nature* **549**, 195 (2017).
- ⁴⁸M. Schuld and F. Petruccione, *Supervised Learning with Quantum Computers*, Quantum Science and Technology (Springer, 2018).
- ⁴⁹V. Havlíček, A. D. Córcoles, K. Temme, A. W. Harrow, A. Kandala, J. M. Chow, and J. M. Gambetta, *Nature* **567**, 209 (2019).
- ⁵⁰G. Kresse and J. Hafner, *Phys. Rev. B* **47**, 558 (1993).
- ⁵¹G. Kresse and J. Furthmüller, *Computational Materials Science* **6**, 15 (1996).
- ⁵²G. Kresse and D. Joubert, *Phys. Rev. B* **59**, 1758 (1999).

Supporting Information for Quantum-inspired Chemical Rule for Discovering Topological Materials

XINYU XU¹, RAJIBUL ISLAM², GHULAM HUSSAIN³, YANGMING HUANG⁴, XIAOGUANG LI³,
PAVLO O. DRAL⁴, ARIF ULLAH^{1,*}, AND MING YANG^{1,*}

¹*School of Physics, Anhui University, Hefei, 230601, Anhui, China*

²*Department of Physics, University of Alabama at Birmingham, Birmingham 35294, AL, USA*

³*Institute for Advanced Study, Shenzhen University, Shenzhen 518060, China*

⁴*State Key Laboratory of Physical Chemistry of Solid Surfaces, College of Chemistry and Chemical Engineering, Fujian Provincial Key Laboratory of Theoretical and Computational Chemistry, and Innovation Laboratory for Sciences and Technologies of Energy Materials of Fujian Province (IKKEM), Xiamen University, Xiamen, 361005, Fujian, China*

**Corresponding authors: arif@ahu.edu.com; mingyang@ahu.edu.cn*

Table of Contents

S1 Derivation of Quantum-inspired Chemical Rule from Quantum–Classical Hybrid Artificial Neural Network	1
S2 Validation of the Quantum-Inspired Chemical Rule Using Complex-Valued Neural Networks	5
S3 Training Details	8
S4 Confidence Analysis of $g^Q(M)$ Score	9

S1 Derivation of Quantum-inspired Chemical Rule from Quantum–Classical Hybrid Artificial Neural Network

In this section, we outline how the chemical rule (Eq. 1 of our main text) emerges from our proposed quantum–classical hybrid artificial neural network (QANN). Our QANN consists of two tightly integrated components—a quantum module and a classical module—as illustrated in Fig. S1.

The quantum module begins with the normalization of input features, which are then encoded into a parameterized Variational Quantum Circuit (VQC) using amplitude encoding. The circuit comprises two main parts: an Encoder, responsible for embedding the classical data into quantum states, and an Ansatz, which forms the trainable section of the circuit. The Ansatz is composed of four identical layers, each containing parameterized Rx and Rz rotation gates, along with CNOT gates that introduce entanglement between qubits. The qubits are subsequently measured, and the measurement outcomes form the latent

quantum representation of the material.

These measured outputs are passed to the classical module, a fully connected neural network that processes the quantum features to predict material properties. The final output layer employs a softmax activation, while model optimization is performed using the cross-entropy loss and Adam optimizer, which jointly update parameters in both the VQC and classical layers through backpropagation. After training for a fixed number of epochs, the optimized parameters are utilized to compute topogivity values for each material.

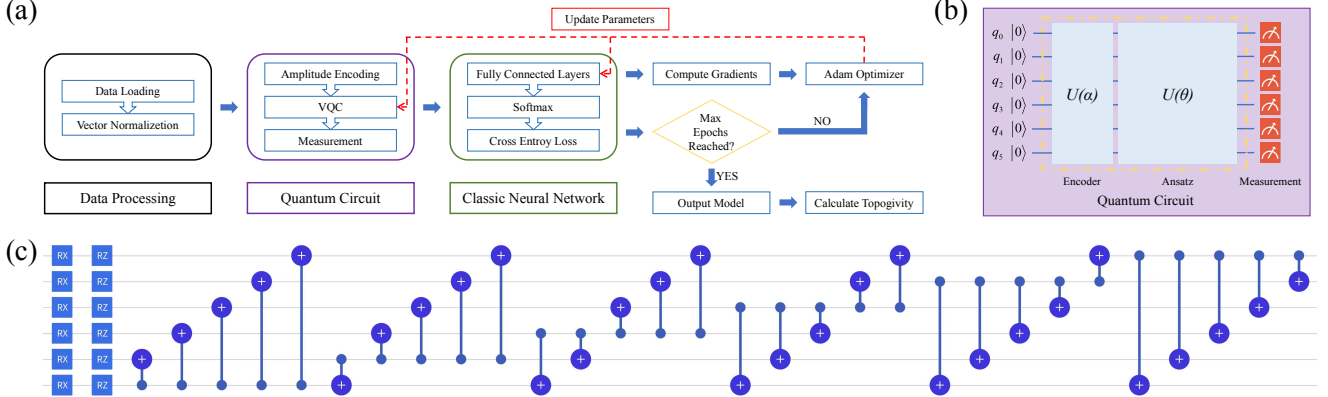


Figure S1: Schematic of the QANN model and quantum circuit. **(a)** In our QANN model, the workflow begins with vector normalization of the loaded data, which is then encoded into a parameterized VQC using amplitude encoding. The output state of VQC is measured, and the results are fed into a classical fully connected neural network. The network’s output is activated by the softmax function, and the cross-entropy loss is computed. The Adam optimizer minimizes this loss via backpropagation, simultaneously optimizing the parameters in both the VQC and the classical network. After a fixed number of epochs (epoch=100), the final model and parameters are saved. These parameters are subsequently used to calculate the topogivity. **(b)** The quantum circuit comprises six qubits ($q_0 - q_5$). The encoder employs the amplitude encoding method, with its circuit corresponding to the unitary matrix $U(a)$, while the ansatz forms the parameterized part of the circuit, corresponding to the unitary matrix $U(\theta)$. Finally, the probability distribution is obtained by measuring the six qubits. **(c)** The depicted layer shows the fundamental structure of the Ansatz circuit. Each horizontal line in the layer represents a qubit. The complete Ansatz comprises four identical such layers, each consisting of parameterized Rx and Rz gates, along with CNOT gates that act as entangling operations.

As input to the QANN model, we define for each material M an elemental composition fraction vector, $\vec{F}(M)$, whose components $f_E(M)$ represent the fractional abundance of each element E in the compound. Elements absent from a material are assigned zero values, whereas those not present in the dataset are excluded from the vector. For the labeled dataset used in this work, $\vec{F}(M)$ is a 54-dimensional vector, corresponding to all unique elements considered, ordered by ascending atomic number for convenience. Mathematically, it can be expressed as:

$$\vec{F}(M) = (f_{Li}(M), f_{Be}(M), f_B(M), f_C(M), \dots, f_U(M))^T. \quad (S1)$$

For notational simplicity, we denote the j -th component of $\vec{F}(M)$ as $f_j(M)$, such that:

$$\vec{F}(M) = (f_0(M), f_1(M), f_2(M), f_3(M), \dots, f_{53}(M))^T. \quad (S2)$$

We then encode $\vec{F}(M)$ into the quantum circuit via amplitude encoding, which requires taking the square root of each component $f_j(M)$ in vector $\vec{F}(M)$. Given that the vector comprises 54 components, a minimum of 6 qubits is necessary (as 6 qubits can encode $2^6 = 64$ data points). This results in 10 unoccupied positions, necessitating a zero-padding operation on $\vec{F}(M)$ by appending 10 zeros, and denote the resulting 64-dimensional vector as $\vec{f}(M)$ leading to:

$$\vec{f}(M) = (\sqrt{f_0(M)}, \dots, \sqrt{f_{53}(M)}, 0, \dots, 0)^T. \quad (\text{S3})$$

The normalized vector $\vec{f}(M)$ is encoded into the quantum circuit through amplitude encoding, initializing from the $|000000\rangle$ computational basis state. The resulting quantum state is prepared as:

$$\begin{aligned} |\psi_{in}\rangle = & \sqrt{f_0(M)} |000000\rangle + \dots + \sqrt{f_{53}(M)} |110101\rangle \\ & + 0 \cdot |110110\rangle + \dots + 0 \cdot |111111\rangle, \end{aligned} \quad (\text{S4})$$

where $\sum_j f_j(M) = 1$. As shown in Fig. S1, the parameterized Ansatz of our QANN employs a fully connected quantum circuit, chosen for its balance between high expressibility and low parameter count. The optimized Ansatz acts as a unitary transformation on the input quantum state $|\psi_{in}\rangle$, such that:

$$U(\theta) |\psi_{in}\rangle = |\psi_{out}\rangle, \quad (\text{S5})$$

which can be expanded into the following form:

$$\begin{bmatrix} u_{0,0} + v_{0,0}i & \dots & u_{0,63} + v_{0,63}i \\ \vdots & \ddots & \vdots \\ u_{63,0} + v_{63,0}i & \dots & u_{63,63} + v_{63,63}i \end{bmatrix} \begin{bmatrix} \sqrt{f_0(M)} \\ \vdots \\ \sqrt{f_{53}(M)} \\ 0 \\ \vdots \\ 0 \end{bmatrix}, \quad (\text{S6})$$

further leading to the output quantum state:

$$|\psi_{out}\rangle = C_0 |000000\rangle + C_1 |000001\rangle + \dots + C_{63} |111111\rangle, \quad (\text{S7})$$

where each complex amplitude is given by:

$$\begin{aligned} C_n &= \sum_{j=0}^{53} (u_{n,j} + v_{n,j}i) \sqrt{f_j(M)} \\ &= \sum_{j=0}^{53} u_{n,j} \sqrt{f_j(M)} + \sum_{j=0}^{53} v_{n,j} \sqrt{f_j(M)} i \\ &= u_n + v_n i. \end{aligned} \quad (\text{S8})$$

Upon measurement, the quantum circuit produces an output probability vector \vec{P} with 64 components, where each component is given by:

$$\begin{aligned}
|C_n|^2 &= |u_n|^2 + |v_n|^2 \\
&= \sum_{j=0}^{53} (u_{n,j}^2 + v_{n,j}^2) f_j(M) \\
&\quad + 2 \sum_{j < k \leq 53} (u_{n,j} u_{n,k} + v_{n,j} v_{n,k}) \sqrt{f_j(M) f_k(M)}.
\end{aligned} \tag{S9}$$

where $n = 0, 1, 2, \dots, 63$. Please note that the second summation term introduces cross terms reflecting interactions among different features—an intrinsic effect arising from quantum measurement. Finally, the resulting probability vector \vec{P} is then used as input to the subsequent classical ANN module.

For the classical ANN module of our QANN model, we adopt a three-layer fully connected architecture. The input layer comprises 64 neurons, corresponding to the 64 components $|C_n|^2$ ($n = 0, 1, 2, \dots, 63$) of the probability vector \vec{P} obtained from the quantum module. The hidden layer contains 24 neurons, while the output layer consists of 2 neurons. A softmax activation function is applied at the output stage to produce normalized classification probabilities. While activation functions are applied during training, they are not strictly necessary for inference in routine material topology prediction. Importantly, the ANN employs only weight parameters (w) and omits bias terms (b), simplifying the network and preserving interpretability.

Data transformation in the ANN occurs through hierarchical propagation across layers, which can be compactly represented as a sequence of matrix multiplications. Let W_1 denote the weight matrix connecting the input and hidden layers, and W_2 the weight matrix connecting the hidden and output layers. Then, for an input vector \vec{C} , the network output can be expressed as

$$\vec{y} = W_2(W_1\vec{C}) = (W_2W_1)\vec{C}, \tag{S10}$$

demonstrating that the overall transformation of the network can be represented by a single effective weight matrix:

$$\begin{aligned}
W_{\text{ANN}} &= W_2W_1 \\
&= \begin{bmatrix} u_{2,0,0} & \dots & u_{2,0,23} \\ u_{2,1,0} & \dots & u_{2,1,23} \end{bmatrix} \begin{bmatrix} u_{1,0,0} & \dots & u_{1,0,63} \\ \vdots & \ddots & \vdots \\ u_{1,23,0} & \dots & u_{1,23,63} \end{bmatrix} \\
&= \begin{bmatrix} w_{0,0} & \dots & w_{0,63} \\ w_{1,0} & \dots & w_{1,63} \end{bmatrix}.
\end{aligned} \tag{S11}$$

We apply this overall parameter matrix W_{ANN} to the vector \vec{P} , obtaining:

$$\begin{aligned}
W_{\text{ANN}}\vec{P} &= \begin{bmatrix} w_{0,0} & \dots & w_{0,63} \\ w_{1,0} & \dots & w_{1,63} \end{bmatrix} \begin{bmatrix} |C_0|^2 \\ \vdots \\ |C_{63}|^2 \end{bmatrix} \\
&= \begin{bmatrix} h_0 \\ h_1 \end{bmatrix},
\end{aligned} \tag{S12}$$

where $h_0 = \sum_{n=0}^{63} w_{0,n} |C_n|^2$, $h_1 = \sum_{n=0}^{63} w_{1,n} |C_n|^2$. These two outputs correspond to the two classification categories of the network (trivial vs. topological). To define a single diagnostic score for material M , we take the difference between these outputs:

$$\begin{aligned}
h(M) &= h_1 - h_0 \\
&= \sum_{n=0}^{63} (w_{1,n} - w_{0,n}) \left[\sum_{j=0}^{53} (u_{n,j}^2 + v_{n,j}^2) f_j(M) \right. \\
&\quad \left. + 2 \sum_{j < k \leq 53} (u_{n,j} u_{n,k} + v_{n,j} v_{n,k}) \sqrt{f_j(M) f_k(M)} \right] \\
&= \sum_E f_E(M) \tau_E + \sum_{E \neq \mathcal{E}} \sqrt{f_E(M) f_{\mathcal{E}}(M)} \tau_{E\mathcal{E}} \\
&= g(M) + \sum_{E \neq \mathcal{E}} \sqrt{f_E(M) f_{\mathcal{E}}(M)} \tau_{E\mathcal{E}} \\
&= g^Q(M),
\end{aligned} \tag{S13}$$

where

$$\tau_E = \sum_{n=0}^{63} (w_{1,n} - w_{0,n}) (u_{n,E}^2 + v_{n,E}^2), \tag{S14}$$

$$\tau_{E\mathcal{E}} = \sum_{n=0}^{63} 2(w_{1,n} - w_{0,n}) (u_{n,E} u_{n,\mathcal{E}} + v_{n,E} v_{n,\mathcal{E}}). \tag{S15}$$

Here, the indices E and \mathcal{E} (with \mathcal{E} running over all elements distinct from E) denote distinct chemical elements within a compound, replacing the earlier indices j and k . The term τ_E describes the self-contribution of element E , while $\tau_{E\mathcal{E}}$ quantifies pairwise correlations between different elements.

Equation (S13) thus yields the quantum-inspired chemical rule $g^Q(M)$ of Eq. 1 (main text). Notably, the same rule—including the correlation terms—can be derived using an equivalent CVNN model, which reproduces the exact analytical structure obtained from the QANN. For completeness, the full derivation is provided in the next section.

S2 Validation of the Quantum-Inspired Chemical Rule Using Complex-Valued Neural Networks

This appendix aims to provide an independent theoretical verification for the quantum-inspired chemical rule extended in the main text by constructing a complex-valued neural network (CVNN). In the QANN framework developed in this work, the core of the quantum circuit is composed of complex unitary matrices, whose weights are inherently complex, naturally enabling the expression of quantum phase interference and coherent superposition. This physical background suggests that if a model is constructed in a purely data-driven manner, complex weights likewise serve as an ideal mathematical mechanism for capturing the deep-seated correlations between material composition and topological properties.

The essence of the CVNN constructed here lies in extending the weights to the complex domain. This is consistent with the mathematical nature of quantum circuits, as both encode phase information and rotational transformations beyond real space through complex operations. This structural homology strongly implies that both the physics-based quantum model and the data-driven complex network lead to the same conclusion: the chemical rules governing the topological properties of materials inherently involve coupling relationships at the complex level among elemental interactions. Therefore, the emergence of the pairwise interaction terms in the chemical rule of Eq. 1 is not accidental but instead a natural consequence of the underlying complex representation shared by both models. To substantiate this claim, we explicitly reconstruct Eq. 1 using the CVNN formalism below.

We begin by specifying the input to the CVNN. For each material M , we introduce an elemental composition fraction vector, $\vec{F}(M)$, whose components $f_E(M)$ represent the fractional abundance of each element E in the compound, just as we did in the QANN model. Elements absent from a material are assigned zero values, whereas those not present in the dataset are excluded from the vector. For the labeled dataset used in this work, $\vec{F}(M)$ is a 54-dimensional vector, corresponding to all unique elements considered, ordered by ascending atomic number for convenience. Mathematically, it can be expressed as:

$$\vec{F}(M) = (f_{Li}(M), f_{Be}(M), f_B(M), f_C(M), \dots, f_U(M))^T. \quad (\text{S16})$$

For notational simplicity, we denote the j -th component of $\vec{F}(M)$ as $f_j(M)$, such that:

$$\vec{F}(M) = (f_0(M), f_1(M), f_2(M), f_3(M), \dots, f_{53}(M))^T. \quad (\text{S17})$$

Unlike the QANN, the input to the CVNN is not constrained by the dimensionality imposed by the number of qubits, so we do not need to zero-pad $\vec{F}(M)$. Furthermore, since the input to the CVNN must be in complex form ($a+bj$), we convert each component $f_j(M)$ in $\vec{F}(M)$ into the complex form $\sqrt{\frac{f_j(M)}{2}} + \sqrt{\frac{f_j(M)}{2}}i$. Consequently, the input vector $\vec{f}(M)$ takes the following form:

$$\vec{f}(M) = (\sqrt{\frac{f_0(M)}{2}} + \sqrt{\frac{f_0(M)}{2}}i, \dots, \sqrt{\frac{f_{53}(M)}{2}} + \sqrt{\frac{f_{53}(M)}{2}}i)^T, \quad (\text{S18})$$

where

$$\sum_j \left| \sqrt{\frac{f_j(M)}{2}} + \sqrt{\frac{f_j(M)}{2}}i \right| = 1. \quad (\text{S19})$$

Our CVNN model adopts a three-layer complex-valued fully-connected architecture. The input layer contains 54 neurons, the hidden layer has 30 neurons, and the output layer consists of 2 neurons. The network outputs a pair of complex numbers. We calculate their squared moduli, which are then processed by a softmax activation function to generate normalized classification probabilities. Although the softmax activation function is used during training, it is not strictly necessary for inference in conventional material topology prediction. It is worth noting that this complex-valued neural network uses only weight parameters (w) and omits bias terms (b), thereby simplifying the network structure and maintaining interpretability.

Similar to any artificial neural network (ANN), data transformation in the CVNN is achieved through layer-wise propagation, which can be compactly represented as a sequence of matrix multiplications. Let W_1 denote the complex-valued weight matrix connecting the input and hidden layers, and W_2 denote the complex-valued weight matrix connecting the hidden and output layers. Then, for an input vector C , the network output can be expressed as:

$$\vec{y} = W_2(W_1\vec{C}) = (W_2W_1)\vec{C}, \quad (\text{S20})$$

demonstrating that the overall transformation of the network can be represented by a single effective weight matrix:

$$\begin{aligned}
W_{\text{CVNN}} &= W_2 W_1 \\
&= \begin{bmatrix} u_{2,0,0} + v_{2,0,0}i & \dots & u_{2,0,29} + v_{2,0,29}i \\ u_{2,1,0} + v_{2,1,0}i & \dots & u_{2,1,29} + v_{2,1,29}i \end{bmatrix} \\
&\quad \times \begin{bmatrix} u_{1,0,0} + v_{1,0,0}i & \dots & u_{1,0,53} + v_{1,0,53}i \\ \vdots & \ddots & \vdots \\ u_{1,29,0} + v_{1,29,0}i & \dots & u_{1,29,53} + v_{1,29,53}i \end{bmatrix} \\
&= \begin{bmatrix} u_{0,0} + v_{0,0}i & \dots & u_{0,53} + v_{0,53}i \\ u_{1,0} + v_{1,0}i & \dots & u_{1,53} + v_{1,53}i \end{bmatrix}, \tag{S21}
\end{aligned}$$

where the indices $0, \dots, 29$ correspond to the hidden-layer with 30 neurons and $0, \dots, 54$ correspond to the input layer. We apply this overall parameter matrix W_{CVNN} to the vector $\vec{f}(M)$, obtaining:

$$\begin{aligned}
W_{\text{CVNN}}\vec{f}(M) &= \begin{bmatrix} u_{0,0} + v_{0,0}i & \dots & u_{0,53} + v_{0,53}i \\ u_{1,0} + v_{1,0}i & \dots & u_{1,53} + v_{1,53}i \end{bmatrix} \\
&\quad \times \begin{bmatrix} \sqrt{\frac{f_0(M)}{2}} + \sqrt{\frac{f_0(M)}{2}}i \\ \vdots \\ \sqrt{\frac{f_{53}(M)}{2}} + \sqrt{\frac{f_{53}(M)}{2}}i \end{bmatrix} \\
&= \begin{bmatrix} \frac{1}{\sqrt{2}} \left(\sum_{j=0}^{53} (u_{0,j} - v_{0,j}) \sqrt{f_j(M)} + \sum_{j=0}^{53} (u_{0,j} + v_{0,j}) \sqrt{f_j(M)}i \right) \\ \frac{1}{\sqrt{2}} \left(\sum_{j=0}^{53} (u_{1,j} - v_{1,j}) \sqrt{f_j(M)} + \sum_{j=0}^{53} (u_{1,j} + v_{1,j}) \sqrt{f_j(M)}i \right) \end{bmatrix} \\
&= \begin{bmatrix} h_0 \\ h_1 \end{bmatrix}. \tag{S22}
\end{aligned}$$

Then, by taking the squared modulus of h_0 and h_1 , we obtain:

$$\begin{aligned}
|h_n|^2 &= |h_{n,\text{real}}|^2 + |h_{n,\text{imag}}|^2 \\
&= \sum_{j=0}^{53} (u_{n,j}^2 + v_{n,j}^2) f_j(M) \\
&\quad + 2 \sum_{j < k \leq 53} (u_{n,j} u_{n,k} + v_{n,j} v_{n,k}) \sqrt{f_j(M) f_k(M)}. \tag{S23}
\end{aligned}$$

These two outputs correspond to the two classification categories of the network (trivial vs. topological). To define a single diagnostic score for material M , we take the difference between these outputs:

$$\begin{aligned}
h(M) &= |h_1|^2 - |h_0|^2 \\
&= \sum_{j=0}^{53} (u_{1,j}^2 + v_{1,j}^2 - u_{0,j}^2 - v_{0,j}^2) f_j(M) \\
&\quad + 2 \sum_{j < k \leq 53} (u_{1,j} u_{1,k} + v_{1,j} v_{1,k} \\
&\quad\quad - u_{0,j} u_{0,k} - v_{0,j} v_{0,k}) \sqrt{f_j(M) f_k(M)} \\
&= \sum_E f_E(M) \tau_E + \sum_{E \neq \mathcal{E}} \sqrt{f_E(M) f_{\mathcal{E}}(M)} \tau_{E\mathcal{E}} \\
&= g(M) + \sum_{E \neq \mathcal{E}} \sqrt{f_E(M) f_{\mathcal{E}}(M)} \tau_{E\mathcal{E}} \\
&= g^Q(M).
\end{aligned} \tag{S24}$$

where

$$\tau_E = u_{1,E}^2 + v_{1,E}^2 - u_{0,E}^2 - v_{0,E}^2, \tag{S25}$$

$$\tau_{E\mathcal{E}} = u_{1,E} u_{1,\mathcal{E}} + v_{1,E} v_{1,\mathcal{E}} - u_{0,E} u_{0,\mathcal{E}} - v_{0,E} v_{0,\mathcal{E}}. \tag{S26}$$

Here, the indices E and \mathcal{E} (with \mathcal{E} running over all elements distinct from E) denote distinct chemical elements within a compound, replacing the earlier indices j and k . The term τ_E describes the self-contribution of element E , while $\tau_{E\mathcal{E}}$ quantifies pairwise correlations between different elements.

The above derivation leads directly to the same chemical rule obtained in Eq. (S13), providing an independent mathematical confirmation from the complex-valued network. The CVNN not only recovers the same pairwise coupling structure as the QANN model but also reveals phase information in the learned complex weights, suggesting that elemental interactions may involve coordinated ‘‘synergistic phases’’ rather than purely additive effects.

Moreover, the complex formulation highlights limitations of real-valued models, which cannot naturally capture such non-commutative interaction patterns. Thus, both the quantum-inspired model and the CVNN converge on the central conclusion: element-pair couplings are indispensable for accurately diagnosing topological materials and form a solid foundation for composition-based topological materials design.

S3 Training Details

The QANN model presented in this work is implemented using VQNet, Origin Quantum’s hybrid quantum-classical machine learning framework.¹ As described in the main text, our full labeled dataset contains 9,026 materials. From this dataset, we selected 8,000 materials for training and set aside the remaining 1,026 as an unseen final test set. To obtain a reliable estimate of model performance and to mitigate overfitting, we applied 10-fold cross-validation to the 8,000-material training subset. Specifically, we divided the 8,000 samples into 10 equal folds (800 materials each). For each of the 10 cross-validation rounds, one fold was designated as the validation set, while the remaining nine folds (7,200 materials) served as the sub-training set. Importantly, in every fold the model was reinitialized with a new random seed and trained entirely from scratch. This procedure produced ten independent sets of learned parameters and ten corresponding validation-set performance metrics.

The validation-set scores reported in our work are the average and standard deviation computed over these ten folds. Thus, each validation score represents a fold-by-fold statistic reflecting how well the model generalizes when trained on 90% of the training data and evaluated on the remaining 10%.

After completing the cross-validation, we combined the ten independently learned parameter sets into a single, final parameter table. Before averaging, each parameter set was normalized relative to the oxygen topogivity value, τ_{O} , which is particularly stable because oxygen appears frequently in the dataset. We first computed the mean oxygen topogivity $\tau_{\text{O,avg}}$ across all ten folds. Then, for each parameter set, we calculated a scaling factor equal to $\tau_{\text{O,avg}}$ divided by its τ_{O} . This scaling factor was applied to all 1,485 parameters in that fold, aligning all parameter sets to a consistent oxygen-normalized reference. Finally, we performed an element-wise average across the ten normalized sets, yielding the final topogivities and inter-element correlation parameters.

These final averaged parameters—not a separately trained model—are then used to compute $g^{\text{Q}}(M)$ for any new material. The final test-set scores reported in the main text are obtained by directly evaluating these final parameters on the 1,026-material test set that was never used during training or cross-validation.

S4 Confidence Analysis of $g^{\text{Q}}(M)$ Score

In this section, we elaborate on the magnitude of $g^{\text{Q}}(M)$ which contains valuable information about the model’s confidence. To quantify this, we introduce a topological confidence score, denoted as $\sigma(B)$, defined for each bin B of $g^{\text{Q}}(M)$ values. Here, a bin represents a specific interval on the real axis of possible $g^{\text{Q}}(M)$ values.

For any bin B , we define:

$$\sigma(B) = \frac{\text{count of topological materials in bin } B}{\text{total number of materials in bin } B}. \quad (\text{S27})$$

Thus, $\sigma(B)$ represents the fraction of materials in bin B that are truly topological according to the ground-truth labels.

To analyze the behavior of this score, we compute the mean and standard deviation of $\sigma(B)$ across all folds in our 10-fold cross-validation. The resulting trend is highly informative as we demonstrate it for our validation and test sets (Fig. S2). When $g^{\text{Q}}(M) < -20$, the topological score remains low and stable, indicating that almost all materials in this range are trivial. In the intermediate region $-20 < g^{\text{Q}}(M) < 20$, the score increases steadily, reflecting growing uncertainty in classification. Once $g^{\text{Q}}(M) > 20$, the score becomes both high and stable, revealing that materials in this range are overwhelmingly topological.

This histogram can also be interpreted directly in terms of classification reliability. For the first five bins (negative $g^{\text{Q}}(M)$ values), the model predicts materials to be trivial. In these bins, $\sigma(B)$ therefore represents the misclassification rate, and the accuracy equals $1 - \sigma(B)$. For the remaining positive-valued bins, the model predicts non-trivial topology, so $\sigma(B)$ directly gives the correct classification rate in that region.

Across both sides of the decision boundary, the classification accuracy improves as $|g^{\text{Q}}(M)|$ increases. This accuracy eventually reaches a plateau once $|g^{\text{Q}}(M)| \approx 20$, beyond which additional increases in magnitude do not significantly change the reliability. This saturation provides strong, quantitative evidence that $|g^{\text{Q}}(M)| \geq 20$ serves as a natural and robust threshold for high-confidence classification, enabling reliable screening in large-scale materials discovery.

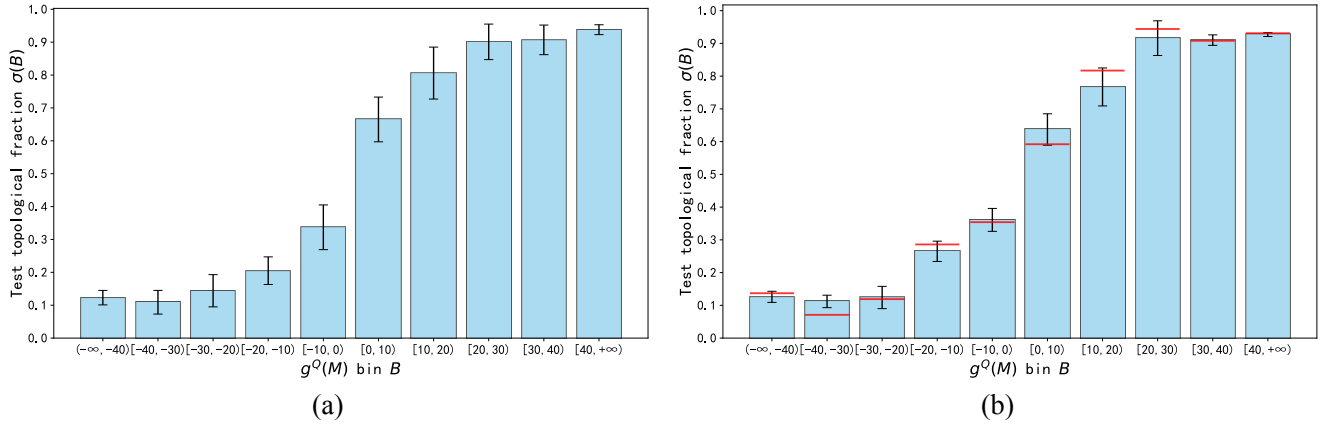


Figure S2: Topological fraction as a function of the $g^Q(M)$ bin. **(a)** Topological fraction vs. $g^Q(M)$ bins evaluated on the validation portions of the 10-fold cross-validation. **(b)** Topological fraction vs. $g^Q(M)$ bins for the final test set. For each bin B , the bar height indicates the mean topological fraction $\sigma(B)$, and the error bars represent \pm one standard deviation. These means and standard deviations are computed from the ten cross-validation folds. In panel (b), the red line shows the topological fraction obtained on the final test set using the aggregated parameter values employed to compute $g^Q(M)$.

References

- [1] Guo, C.; Liu, J.; Li, L.; Gao, Y.; Wang, X.; Zhao, Q.; Xie, Y.; Wei, Z.; Zhang, Z.; Liu, T.; others VQNet: Library for a Quantum-Classical Hybrid Neural Network. *arXiv preprint* **2020**, Submitted on 9 Jan 2020, v1.